Discover Nano

Research

Fabrication of lipid-modified drug nanocrystals loaded injectable hydrogel for breast cancer therapy

Manish Kumar[1,2] · Abhishek Jha[1,3] · Pooja Goswami[4] · Ritika Srivastava[1] · Manjit Manjit[1] · Kanchan Bharti[1] · Biplob Koch[4] · Brahmeshwar Mishra[1]

Received: 6 October 2024 / Accepted: 3 February 2025
Published online: 12 February 2025

Abstract
The current study includes the design of soluplus stabilized, lipid-coated, and fucoidan-oleylamine conjugate modified paclitaxel nanocrystals. The nanocrystals (Lipid-NCs) were about 100 nm, homogeneous, stable and showed improved drug release compared to pure PTX. The nanocrystals were subsequently loaded in an in situ gel-forming hydrogel for the intratumoral injection. The resulting hydrogel exhibited a sol-form at the lower temperature of 2–8 °C while converted to a gel-form at the body temperature. The injectable hydrogel had a reasonable viscosity, an acceptable pH, good syringeability, and a quick sol–gel transition. The hydrogel demonstrated high payload potential, homogeneous distribution, and controlled long-term drug release. In vivo studies revealed the higher efficacy of Lipid-NCs hydrogel in tumor inhibition while avoiding systemic toxicity, compared to pure PTX-loaded hydrogel and intravenously administered PTX. In conclusion, nanocrystal-loaded hydrogel is a promising localized drug delivery system for breast cancer therapy.

Keywords Nanocrystals · Hydrogel · Implant · Drug delivery · Breast cancer

1 Introduction

Breast cancer is one of the most common and aggressive types of cancer worldwide, with a high fatality rate [1]. Surgical resection of local breast tumor is the preferred treatment but has a high risk of incomplete tumor removal and surgical complications [2]. These can lead to induction of several pathophysiological processes that trigger the tumor recurrence, resulting in surgery induced-metastasis [3, 4]. The conventional treatment includes the intravenous administration of anticancer drugs; however they are associated with drug distribution to major organs of body, systemic toxicity, limited drug availability at tumor site, poor therapeutic effects, occurrence of drug resistance and advancement of cancer to metastases [5–7]. Therefore, strategies for maximizing the drug availability at tumor site are required to prevent

Supplementary Information The online version contains supplementary material available at https://doi.org/10.1186/s11671-025-04195-w.

✉ Brahmeshwar Mishra, bmishra.phe@iitbhu.ac.in; Manish Kumar, manishkumar.rs.phe19@itbhu.ac.in; Abhishek Jha, abhishekjha.phe17@itbhu.ac.in; Pooja Goswami, pooja1428@bhu.ac.in; Ritika Srivastava, ritika.srivastava@iitgn.ac.in; Manjit Manjit, manjit.rs.phe20@itbhu.ac.in; Kanchan Bharti, kanchan.bharti.rs.phe18@itbhu.ac.in; Biplob Koch, biplob@bhu.ac.in | [1]Department of Pharmaceutical Engineering and Technology, Indian Institute of Technology (BHU), Varanasi, Uttar Pradesh 221005, India. [2]Amity Institute of Pharmacy, Amity University, Greater Noida, Uttar Pradesh 201308, India. [3]Department of Pharmaceutics, Dr. D. Y. Patil Institute of Pharmaceutical Sciences and Research, Pimpri, Pune 411018, Maharashtra, India. [4]Genotoxicology and Cancer Biology Laboratory, Department of Zoology, Institute of Science, Banaras Hindu University, Varanasi, Uttar Pradesh 221005, India.

postoperative cancer recurrence. In this regard, localized drug delivery systems have been observed more effective by maintaining drug concentration at target site for a prolonged period, minimizing organ distribution and thus diminishing systemic side effects [8, 9]. Recently, injectable hydrogels have been reported by many research scientists for the localized drug delivery and cancer therapy [10–12]. Injectable hydrogels exhibiting sol–gel transition at body temperature has been reported for various anticancer drug delivery applications. These consists of polymers that remain in sol-form suitable for injection and converts to gel-form at a physiological body temperature. The thermo-reversibility of hydrogel offers the advantages of easy administration via injection, gel-depot formation at tumoral tissues and extended residence at target site for continuous drug release [13].

Considering all the above facts, the objective of present work was formulation of paclitaxel loaded thermosensitive hydrogel for localized drug delivery and breast cancer therapy. Such hydrogel acts an effective drug carrier for intratumoral injection to form depot and provide controlled release at tumor region. However, PTX belonging to Biopharmaceutics Classification System (BCS) class IV exhibits low solubility and poor penetration, thereby hampering the drug release [14]. To improve the drug efficacy, PTX can be fabricated as nanocrystals. Nanocrystals owing to their size and surface properties withhold higher aqueous solubility and greater tumor tissues penetration. Additionally, lipid-coated nanocrystals (Lipid-NCs) can be prepared, further facilitating the fusion of lipid-particles with cancer cell membranes and hence promoting the intracellular drug delivery via phospholipid bilayer diffusion [15]. Lipid-NCs can control the drug release responsible for retaining maximum drug at site and can be equipped with molecules having selectivity towards cancer cells. Therefore, present work involved fabrication of PTX as drug nanocrystals using soluplus as stabilizer, soya-lecithin (SLec), cholesterol (Chol) & tocopherol polyethylene glycol succinate (TPGS) as lipid-membrane materials, and amphiphilic fucoidan-olylamine (FP-OA) conjugate as targeting moiety. Fucoidan are sulphated polysaccharides with high affinity towards cell surface receptors overexpressed on tumor cells [16]. Then, drug and nanocrystals were loaded in thermosensitive injectable hydrogel constructed with chitosan and pluronic F127 to give PTX-Gel, SPNC-Gel, and Lipid-NCs-Gel. The purpose was to investigate the effect of drug nanocrystals in improving therapeutic efficacy of drug towards management of breast cancer. Prepared nanocrystals and nanocrystals loaded hydrogels were evaluated for physicochemical, in vitro and in vivo anti-tumor characteristics.

2 Experimental

2.1 Materials required

Fucoidan (Undaria pinnatifida) of medicine grade (98% fucoidan) was received as a gift sample from Nutra Green Biotechnology, Co., Ltd. Shanghai Lvshang Biotechnology, Shanghai-200129, China. Oleylamine, N-Ethyl-N'-(3-dimethylaminopropyl) carbodiimide (EDC), and N-Hydroxysuccinimide (NHS) were procured from SRL Pvt. Ltd. Paclitaxel (USP, 98–100%) was gifted by MSN Laboratories Pvt. Ltd., Unit II, Sy No: 50, Kardanur, Medak (Dist.), Telangana, India. Vitamin E TPGS NF Grade was procured from Antares Health Products, St. Charles, USA. A gift sample of soybean lecithin (SLec) was obtained from Lipoid, GmBH. Cholesterol extrapure AR, 99% (Chol), medical grade chitosan (Mwt, 100–300 kDa and 95% acetylation degree), and Pluronic F127 (Mwt 12,000 Da) were purchased from SRL chemicals, India. All the solvents used in the experiments were of HPLC grade.

The MDA-MB-231 cell line was obtained from NCCS Pune, India. DMEM and 12-well culture plates were purchased from Genetics Biotech Asia Pvt. Ltd., while T-25 flasks were sourced from Eppendorf. Penicillin–streptomycin, Trypsin–EDTA, and FBS were acquired from Gibco. PBS was prepared using high-quality chemicals from a reputable brand, and Hoechst 33,342 and PI were obtained from Realgene.

2.2 Synthesis and characterization of fucoidan-oleylamine conjugate

Fucoidan-oleylamine conjugate was synthesized using a two-step procedure (Fig. S1). Firstly, 1 g of fucoidan was added to 20 ml of distilled water and kept under stirring on ice-bath. 40 mg of sodium hydroxide was added to the mixture followed by 95 mg of chloroacetic acid and maintained on stirring for 6 h. The reaction mixture was then subjected to dialysis using membrane with MWCO 1 kDa for 48 h in distilled water followed by lyophilization to yield carboxymethyl-fucoidan. The activation of carboxyl groups on the carboxymethyl fucoidan was done using the EDC/NHS solution. 1 g of carboxymethyl fucoidan was added to 10 ml of distilled water followed by addition of EDC HCl (192 mg) and NHS (230 mg). The reaction mixture was kept on stirring at room temperature for 3 h followed by the dropwise addition of 350 µl of oleylamine (eq. to

1 mmol) diluted in 9.65 ml of ethanol. The reaction was allowed to continue for 48 h at the room temperature. The resultant mixture was then dialyzed for 24 h with 50% ethanol followed by distilled water for 48 h to remove EDC, NHS, and oleylamine. The purified mixture was lyophilized to obtain the fucoidan-oleylamine conjugate (yield 48.92%). The synthesis of fucoidan-oleylamine conjugate was confirmed by 1H NMR. The conjugate and oleylamine were dissolved in d6-DMSO and fucoidan was dissolved in D_2O. The 1H NMR spectra was obtained on AVH D 500 AVANCE III HD (500 MHz OneBay NMR Spectrometer; BRUKER BioSpin International AG). FTIR analysis were conducted by KBr pellet method on Nocolet iS5 (Thermo Electron Scientific Instruments LLC).

2.3 Formulation of paclitaxel nanocrystals

Paclitaxel nanocrystals were prepared by antisolvent crystallization followed probe sonication method [17, 18]. Briefly, 10 ml of soluplus solution (0.5% w/v) was prepared as an aqueous dispersion medium to which 20 mg/ml ethanolic PTX solution as an organic phase was added by drop-by-drop method. The system was maintained under continuous stirring at 2000 rpm on a magnetic stirrer and at a lower temperature on ice-bath. Stirring assisted the rapid and uniform diffusion of drug from the organic phase to the aqueous phase where lower temperature induced the drug nucleation to give drug nanocrystals simultaneously stabilized with polymer soluplus. Resultant nanocrystals were probe-sonicated for 5 min * 2 at an amplitude of 60% to obtain paclitaxel nanocrystals (SPNC). For preparation of lipid-modified paclitaxel nanocrystals (Lipid-NCs), the organic phase consisting of PTX (10 mg), SLec (6 mg), Chol (3 mg) and FP-OA (3 mg), in ethanol/chloroform was used. The organic phase was added to 1% w/v soluplus aqueous phase and probe sonicated for 10 min. Resultant nanosuspension were stirred overnight at 25 ℃ and centrifuged at 15,000 rpm for 10 min to collect the nanocrystals.

2.4 Characterization of nanocrystals

2.4.1 Particle analysis

The particle size, polydispersity index (PDI) and zeta-potential were analyzed by Malvern Master sizer based on Dynamic light scattering (DLS) principle. The sample was diluted 20-fold and sonicated for 2 min to disperse the particles uniformly. Measurements were taken at room temperature in triplicates.

2.4.2 Entrapment efficiency, and drug loading

The drug loading and entrapment efficiency were determined using High-Performance Liquid Chromatography (HPLC, Shimadzu, Japan) method using C18 column (150 mm length, 4.6 mm diameter, and 5 µm particle size) and mobile phase of Acetonitrile (ACN) and water at 0.6 and 0.4 volume fractions, respectively. The flow rate was maintained at 1 ml min^{-1} and the wavelength of 229 nm was used. The calibration curve was linear in the range of 10–100,000 ng/mL with a correlation coefficient of $R^2 = 0.999$ [18].

$$\text{Drug loading} = (\text{Total amount of PTX in NCs/Total weight of PTX} + \text{Excipients}) \times 100.$$

$$\text{Entrapment efficiency} = (\text{Total amount of PTX in NCs/ Initial amount of PTX}) \times 100.\text{Entrapment efficiency} = (\text{Total amount of PTX in NCs/ Initial amount of PTX}) \times 100.$$

2.4.3 Stability study

To predict the colloidal stability of nanocrystals, lyophilized samples stored in refrigerator were analyzed for particle size, PDI and zeta potential [19]. For this, samples were resuspended in PBS and measured in triplicates at predetermined time intervals (day 1, 7, 15, 30, 90, and 180). The entrapment efficiency was also determined at day 1, 30, 90 and 180.

2.4.4 Microscopy (SEM, AFM and TEM)

The morphology of SPNC and Lipid-NCs was evaluated by Scanning Electron Microscope (SEM, Nova Nano SEM 450, FEI, USA), Scanning Probe Microscope (SPM/AFM, NTEGRA Prima, NT-MDT Service & Logistics Ltd.) and Transmission electron microscopy (TEM; TechnaiG2 20 TWIN, FEI, USA).

2.4.5 Spectroscopy (FTIR, XRD, DSC, XPS)

Fourier-transform infrared (FT-IR) spectra of pure PTX, SPNC, Lipid-NCs were acquired using a JASCO FT/IR-4200 type A (JASCO Co., Tokyo, Japan) in the range 600–4000 cm^{-1}. Differential scanning calorimetry (DSC) was performed using DSC-60 Plus (Shimadzu, Asia Pacific). X-ray diffraction (XRD) analysis was done using Rigaku Miniflex 600 Desktop X-Ray Diffraction System (RIGAKU Corporation) using monochromatic CuKα-radiation (λ = 1.5406 Å) at 40 kV over a range of 2θ angles from 0 to 50° with step size of 0.02°/s and scan speed of 5°/min. X-ray photoelectron spectroscopy (XPS) was used to assess the surface chemistry of formulations using K-Alpha (Thermo Fisher Scientific) with Mg Kα radiation (hν = 1253.6 eV) in the range of 100–700 eV binding energy.

2.4.6 In vitro *drug release study*

Drug release study of pure PTX, SPNC and Lipid-NCs was conducted by dialysis membrane method. PBS pH 6.8 was used as the release medium maintained at 37 ± 0.5 °C under continuous stirring at 50 rpm and 1% tween 80 was used to maintain the sink condition [18]. The release profiles were fitted to various kinetic models for determining the release mechanism (details in supplementary).

2.4.7 In vitro *cell line studies*

Cell line maintenance: The MDA-MB-231 cell line was incubated in a controlled environment at 37 °C in a humidified CO2 incubator. The cells were cultured in DMEM with FBS, and a penicillin–streptomycin solution was added to prevent bacterial contamination. These optimal conditions supported the growth and propagation of the cells.

MTT assay: The cytotoxicity of pure PTX, Placebo (soluplus + lipid mixture), SPNC, Lipid-NCs (without FP-OA), and Lipid-NCs (with FP-OA) was evaluated by MTT assay. MDA-MB-231 cells were plated in 96 well culture plate at a density of 5×10^5 cells for 24 h to adhere followed by treatment with the samples (0.1–5 µg/ml). The cells were incubated for 48h and afterward wells were washed with PBS. Then, 100 µl of MTT solution (0.5 mg/ml) was added followed by incubation for 4 h and solubilization of formazan crystals with DMSO (100 µl). The plates were read at 570 nm using microplate reader.

Cellular uptake: For cellular uptake study in MDA-MB-231 cells, free coumarin-6 (C6), pure PTX-C6, SPNC-C6, Lipid-NCs-C6 (without FP-OA), and Lipid-NCs-C6 (with FP-OA) were used. C6 equipped nanocrystals were produced by using 1 mg of C6 along with 10 mg PTX in organic phase, and rest procedure is followed as described above to obtain SPNC-C6 and Lipid-NCs-C6. To assess cellular internalization potential of SPNC-C6, Lipid-NCs-C6 (without FP-OA), and Lipid-NCs-C6 (with FP-OA) as compared to free C6, and pure PTX-C6, this study was conducted. For this, approximately 30×10^3 cells were seeded on coverslips in a 12-well plate and incubated for 12 h in a 5% humidified CO_2 incubator. After discarding the spent media, the cells were counterstained with DAPI (20 µg/ml). Images were captured using an inverted fluorescence phase contrast microscope (EVOS FL) at 400X magnification.

Apoptosis study through Hoechst 33342/PI dual staining method: Hoechst 33342/PI dual staining was performed to evaluate the impact of Placebo (soluplus + lipid mixture), SPNC, Lipid-NCs (without FP-OA), and Lipid-NCs (with FP-OA) drug on nuclear morphology and condensation, as compared to pure PTX. Approximately 30×10^3 cells were plated in a 12-well plate with complete media. After the cells attained the appropriate morphology, they were treated with Blank and all samples at the IC_{50} concentration of Lipid-NCs (with FP-OA) and incubated for 24 h. The cells were then stained with Hoechst 33342 (10 µg/ml) and PI (5 µg/ml) for 15 min, and images were captured using an inverted fluorescence phase contrast microscope at 400X magnification.

2.5 Formulation of in-situ hydrogel

The injectable hydrogel was fabricated using Pluronic F127 and chitosan [20]. For this, 10 ml of 3% w/w medium molecular weight chitosan solution was first prepared in 0.1 M acetic acid by stirring for 30 min. The aqueous solution (20 ml) of 30%

w/w Pluronic F127 was added gradually to previously prepared chitosan solution maintained at 0–4 ℃ on ice bath under continuous stirring. The mixture was further stirred for about 30 min to obtain uniformly dispersed continuous hydrogel. The prepared hydrogel was then centrifuged at 12,000 rpm to remove the air bubbles and stored in the refrigerator at 8 °C until further experiments. For preparation of nanocrystals loaded hydrogel, nanocrystals powder (equivalent to 1% w/v PTX) was added to hydrogel-base maintained at a lower temperature on ice bath under continuous stirring to homogeneously disperse the nanocrystals. The gelation process was further done at 30 °C and the repeated 3 cycles of sol–gel transition were employed to obtain the final product [21].

2.6 Evaluation of in-situ hydrogel

2.6.1 Microscopy

SEM and AFM analysis was done for nanocrystals-free Gel and nanocrystals-loaded Gel. For this, hydrogel was diluted using distilled water and a thin film over glass slide was prepared, lyophilized to form the dry film. The dry film was coated with gold for SEM analysis.

2.6.2 Sol–gel transition

The gelation temperature of prepared in-situ hydrogel was determined by recording the temperature (Tgel) at which sol–gel transition occurs when heated over a magnetic stirrer. The gelation was confirmed when the magnetic bar stopped due to the gel-resistance. The sol–gel phase transition was also investigated by vial-tilt method and gelation time was noted as the time taken to reach the state when solution stop to flow for 1 min after inverting the vial [20]. For this, cold gel in a glass vial was gradually heated upto 37 °C on a water bath. After each minute, the glass vial was removed and inverted for 1 min to check the gel formation.

2.6.3 Rheology and syringeability

The viscosity of sol and gel-form was measured by Anton Paar-viscometer (MCR 72 EDU Edition). The injectability performance was conducted by filling cold-gel (sol) in a syringe (24G) and then injecting out the cold-gel over the petri plate at room temperature [22].

2.6.4 Visual inspection, pH determination and drug content uniformity

Produced hydrogels were evaluated for clarity, pH, phase separation, and homogeneity in either gel or sol forms. Physical inspections like color and texture of the gel was done visually while pH measurement was conducted using a digital pH meter [23]. To determine the drug content, the samples (1 g) were added to distilled water: methanol (1:1) and vortexed for 10 min followed by 15 min ultrasonication to disrupt the hydrogel integrity and dissolve the loaded drug or nanocrystals. The resulting mixture was filtered and investigated at λ_{max} 229 nm using HPLC. The hydrogel drug content uniformity was determined by analyzing the top, middle and bottom layers of hydrogel [17].

2.6.5 In vitro *drug release*

For PTX release study from SPNC Gel and Lipid-NCs Gel, dialysis method was employed [21]. The hydrogel (1 mL) was sealed in dialysis bag and maintained at 37 °C to ensure sol–gel transition. Then, dialysis bag with hydrogel sample was suspended in a pH 6.8 PBS (release medium) and kept under stirring at 200 rpm at 37 ± 0.5 °C. An aliquot of 1 ml was collected at predetermined intervals and replaced with fresh PBS solution. The drug quantification in each withdrawn sample was done by HPLC method, as aforementioned. The drug release profile was fitted to various release kinetic models for determining the release mechanism (Detail In supplementary, Table S1).

2.7 In vivo *studies*

In vivo experiments protocol was approved by Institutional Animal Ethics Committee (IAEC) at Indian Institute of Technology (BHU) Varanasi (Approval No.: IIT(BHU)/IAEC/2023/015) and were in accordance with CPCSEA (a Committee

for the Purpose of Control and Supervision of Experiments on Animals in India; Regd. No.: 2123/GO/Re/S/21/CPCSEA). All procedures performed in the study were in accordance with the ARRIVE guidelines. Breast tumor model was developed in post-weaning pre-pubescent (5 weeks old) female Sprague Dawley (SD) rats acclimatized for seven days. DMBA (65 mg kg^{-1}) in corn oil was administered subcutaneously close to breast pads for tumor induction. The tumor of about 10 ± 1.5 mm) was confirmed post 10–12 weeks of DMBA administration. The DMBA-induced tumor-bearing female SD rats were then divided into four groups (n = 5) [23]. First group received no treatment and denoted as untreated tumor bearing SD rats, while second group was PTX (i.v.) administered intravenous dose of 8 mg/Kg/day PTX in Cremophor EL: Etthanol (1:1) diluted in saline. The third and fourth group were PTX Gel and Lipid-NCs Gel, administered as in-situ hydrogel forming injectable formulation (equivalent to 8 mg/Kg/day PTX) [21]. The formulations were administered at day 0, 3, 6, 9, and 12 while the measurements of body weight and tumor diameter were done at day 0, 4, 7, 10, and 14. The tumor volume was calculated using the formula below; where r was average radius of the tumor.

$$\text{Tumor volume} = 4/3 \prod r^3.$$

For histological analysis, tumor and organs were harvested at day 14. Then, organs were fixated in formalin, embedded in paraffin, sectioned, and mounted on glass slides followed by staining with haematoxylin and eosin (H&E). The tissue samples were mounted under a coverslip and observed under light microscope. The survival analysis was investigated using five Groups (n = 5) consisting of healthy SD rats along with other four groups as mentioned above, housed for 120 days [24].

2.8 Statistical analysis

Each experiment was conducted in triplicates and results were reported as Mean ± standard deviation (SD). The statistical significance was ascertained through t-test (non-parametric), one-way ANOVA and two-way ANOVA at p values of $^{*}p < 0.05$, $^{**}p < 0.01$, $^{***}p < 0.001$, and $^{****}p < 0.0001$. The analysis was performed using GraphPad Prism 9.0.0 for windows (GraphPad Software, San Diego, CA, USA).

3 Results and Discussion

3.1 Characterization of fucoidan-oleylamine conjugate

In 1H NMR spectrum of fucoidan (Fig. 1A), an intense singlet peak of shielded protons at around 1.29 ppm was assigned to $–CH_3$ groups (H-6 at C-6 carbons) of the l- fucopyranose. The spectrum also contained resonance characteristics of fucoidan with signals from ring protons (H-2 to H-5 bonded to C-2 to C-5 carbons) at 3.5–4.5 ppm [25]. This confirmed the presence of different types of fucosal sulfate groups with changes in glycosidic linkage positions and monosaccharide patterns. The chemical shifts ranging from 5.0 to 5.5 ppm were attributed to anomeric protons ($H1_{\beta}$) of β-linked sugars and ($H1_{\alpha}$) of α-linked-l-fucose [26]. The peaks were similar to previously reported spectrum for fucoidan [16, 27]. The characteristic proton signals of oleylamine and Fucoidan -oleylamine conjugate were as shown in Fig. 1B and C, respectively. The amide bond formation between fucoidan and olelylamine was confirmed by peak at 1.97 for proton attached to NH_2 bonded carbon of amide. The results are further confirmed using FTIR analysis (Fig. 3A). The fucoidan showed characteristic IR bands at 3440 cm^{-1} (O–H group of monomeric monosaccharides), 2940 cm^{-1} (C–H stretching), 1645 cm^{-1} (C = O stretching), 1257 cm^{-1} (asymmetric stretching of S = O), 1052 cm^{-1} (ether bond C–O, RO-SO3), and 850 cm^{-1} (C–O–S of sulfate ester groups) [25, 26, 28, 29]. Fucoidan-oleylamine conjugate showed peak band at 3007 cm^{-1} (= C–H bending of OA), 2923 cm^{-1} (asymmetric C-H Stretching of OA), 2856 cm^{-1} (symmetric C–H Stretching of OA), 1737 cm^{-1} (C = O stretch, amide bond), 1461 cm^{-1} (CH3 bending of OA), 1370 cm^{-1}, 1254 cm^{-1} (asymmetric stretching of S = O of FP), 1067 cm^{-1} (C-N bending) and 864 cm^{-1} (C–O–S bending of sulfate ester groups of FP) [28]. This confirmed the conjugation of fucoidan with olelylamine through amide bond formation to give the amphiphilic conjugate.

3.2 Characterization of nanocrystals

The present work involved synthesis of paclitaxel nanocrystals surface coated with polymer and lipid materials. Soluplus was employed as stabilizer for nanocrystals (SPNC) preparation, while soy lecithin as main lipid material was used along

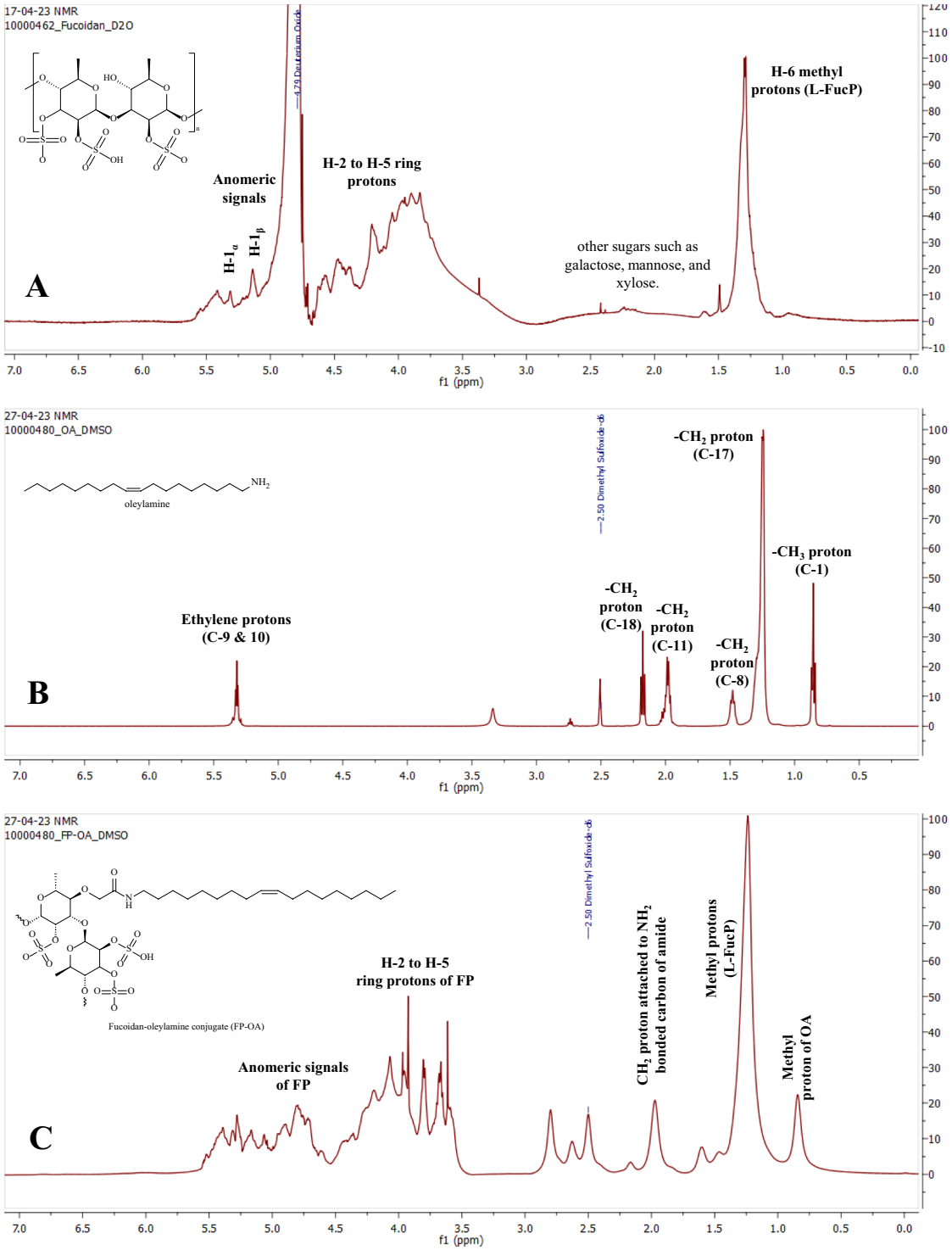

Fig. 1 NMR Spectra of fucoidan (**A**), oleylamine (**B**), and fucoidan-oleylamine conjugate (**C**)

with stabilizer soluplus for fabrication of lipid-coated nanocrystals (Lipid-NCs). The nanocrystals were prepared by antisolvent crystallization followed probe sonication method. The cold temperature assisted the drug nucleation to give drug crystals that were simultaneously stabilized with stabilizer soluplus. The resultant drug nucleated crystals were probe sonicated to get nano-sized drug crystals. The drug nanocrystals were of particle size 69.29 ± 11.10 nm and 111.9 ± 32.40 nm as observed for SPNC and Lipid-NCs, respectively. The nanocrystals were homogeneously dispersed particles with polydispersity index (PDI) of 0.106 ± 0.029 (SPNC) and 0.147 ± 0.012 (Lipid-NCs). The nanocrystals were anionic in nature

with Zeta potential of −8.81 ± 2.26 mV for SPNC and −10.3 ± 2.94 mV for Lipid-NCs (Fig. S2). The anionic charge could be due to stabilizer polymer and lipid material used for surface coating of drug nanocrystals. The charge was sufficient to avoid nanocrystals aggregation and maintain the monodispersed particulate system. Prepared nanocrystals also had high encapsulation efficiency (EE) of 94.76 ± 3.87% and 85.23 ± 4.54%, while drug loading (DL) 26.18 ± 2.10% and 12.63 ± 4.27% for SPNC and Lipid-NCs, respectively. The nanocrystals were stable during storage and were resistant to change in particle size, PDI, zeta potential and EE (Fig. 2A–D). Microscopy studies revealed cubic to rectangular shaped nanocrystals of about 60.11 ± 10.95 nm for SPNC and spherical shaped particles of about 129.48 ± 36.85 nm for Lipid-NCs, as observed in SEM (Fig. 2E and H). The increase in size could be due to lipid coating material. The nanocrystals were smooth surfaced as observed in AFM (Fig. 2F and I). The size of nanocrystals was in accordance to SEM, as confirmed by TEM (Fig. 2G and J).

The spectroscopic analysis including FTIR, XRD, DSC and XPS was further conducted for PTX, SPNC and Lipid-NCs. FTIR spectrum (Fig. 3B) of pure PTX showed characteristic absorption peaks at 1734 cm^{-1} (C = O stretching vibration), 1707 cm^{-1} (C = O stretching vibration of ester group), 1646 cm^{-1} (C–C stretch), 1244 cm^{-1} (C-N stretching) and 709 cm^{-1} (C–H off the plane) [19]. SPNC exhibited IR bands at 3480 cm^{-1} (OH stretch of Soluplus), 2920 cm^{-1} (–CH stretch), 1736 cm^{-1} and 1625 cm^{-1} (–C = O stretch), 1245 cm^{-1} (–C–O stretch), and 714 cm^{-1}. This suggested encapsulation of PTX in Soluplus matrix. Whereas, Lipid-NCs had IR bands at 3440 cm^{-1} (OH stretch of TPGS/SLec), 2922 cm^{-1} (alkyl -CH stretching of SLec/FP-OA), 2853 cm^{-1} (symmetric C-H Stretching of FP-OA) 1740 cm^{-1} (–C = O stretching vibration of SLec/FP-OA) 1467 cm^{-1} (C–H stretching vibration of methyl group in SLec), 1375 cm^{-1} (–CH2 group), 1240 cm^{-1} (P = O stretching vibration of SLec, S = O stretching), 1097 cm^{-1} (–O–C stretching vibration of SLec), 865 cm^{-1} (C–O–S bending of FP) [28]. The results confirmed coating of SPNC surface by SLec and FP-OA.

XRD spectrum of PTX, SPNC and Lipid-NCs is represented in Fig. 3C. Diffraction pattern of PTX showed characteristic peaks at 2θ of 5.712˚, 9.0156˚, 10.126˚, 11.346˚, 12.531˚, 14.011˚, 14.756˚, 15.750˚, 17.180˚, 18.067˚, 18.843˚, 19.85˚, 21.141˚, 22.085˚, 22.911˚, 25.331˚, 27.269˚, 28.782˚ and 30.057˚, implying high crystallinity [19]. SPNC showed a broad amorphous peak of soluplus suggesting conversion of crystalline drug to amorphous particles. While Lipid-NCs showed diffraction pattern at 2θ = 5.41˚, 12.72˚, 14.16˚, 15.39˚, 17.07˚, 19.11˚, and 23.07˚. The broad high intensity peaks at 19.11˚ and 23.07˚ correspond to SLec while peaks at 5.41˚, 12.72˚ and 17.07˚ were attributed to FP-OA. The other peaks 14.16˚ and 15.39˚ were for Chol. The results confirmed the coating of SPNC nanocrystals surface with lipid layer and FP-OA.

DSC thermogram of pure PTX, SPNC and Lipid-NCs is shown in Fig. 3D. Pure PTX found to have an endothermic peak at 224 °C corresponding to melting of crystalline drug [19, 30]. The endothermic peak of PTX was absent in SPNC attributed to amorphosization of crystalline drug particles by amorphous soluplus. In addition, lipid coated nanocrystals also absent PTX endotherm, showing peaks at 39 °C, 64–80 °C, 200 °C, and 280 °C corresponding to TPGS melting, Chol, SLec fusion and SLec decomposition, respectively. This suggested successful coating of lipids on nanocrystals surface without disruption of nanocrystals integrity.

The surface functionalization of fucoidan on Lipid-NCs was further confirmed by a detailed analysis of S2p, C1s, N1s and O1s lines of the XPS spectrum (Fig. 4A). Deconvolution of S2p spectral peak for fucoidan (FP) showed two sulfur chemical environments at approximately 168.15 eV (for –SO3– group) and 169.37 eV (for interacting –OSO3– group), similar to previous reports [29]. The results were similar to previously reported data for fucoidan [31]. Alteration in FP-OA spectra was due to conjugation of oleylamine to fucoidan, however the peaks of fucoidan were at similar position. For Lipid-NCs, one sulfur environment was observed, at binding energies of 168.28 eV (–SO3– group) [25]. Change in binding energy peak and disappearance of -OSO3 peak was attributed to fucoidan-olylamine conjugate, while detection of peak confirmed the presence of fucoidan on Lipid-NCs surface [25, 28, 29]. The C1s spectral peaks of fucoidan was observed at 284.19 eV (C–C, C–H), 285.68 eV (C–O, C–OH) and 287.30 eV (O–C = O, C = O) [25]. For lipid NCs, C1s peaks at around 284.31 eV, 285.73 eV and 287.78 eV confirming presence of fucoidan on nanocrystals surface [25]. The N1s peak for fucoidan was observed as single peak at 399.28 eV while Lipid-NCs showed three peaks. The peaks at 399.03 eV confirmed presence of fucoidan at nanocrystals surface while two extra peaks at 400.87 eV, and 402.02 eV were attributed to lipid coating material (Slec and FP-OA). O1 peak of fucoidan was observed as doublet at 530.68 eV and 532.08 eV which appeared with altered intensity at 530.30 eV and 532.07 eV for lipid-NCs attributed to incorporated FP-OA. In addition to S2p peak, P2p peak was also present in Lipo-NCs XPS confirming surface coating of SPNC with lipid materials (FP-OA & SLec) (Fig. 4B).

The release curve of free PTX, SPNC and Lipid-NCs at pH 6.8 is also provided in Fig. 4C. The release rate of free PTX was slow, exhibiting only 23.90 ± 2.22% drug release in 24 h. Pure PTX followed Makoid-Banakar release model (n = 0.75 and kMB = 3.2) model. Since the diffusion index n was 0.75 (i.e., 0.45 < n < 0.89), the drug release was expected via erosion as well as diffusion [32, 33]. SPNC and Lipid-NCs in contrary showed significantly higher PTX release of 99.98 ± 3.59% and 75.63 ± 3.92%, respectively in 24 h. Higher drug release from nanocrystals at target site can favor in maintaining the drug concentration gradient at tumor tissues to exert therapeutic action. However, too fast release can also result in

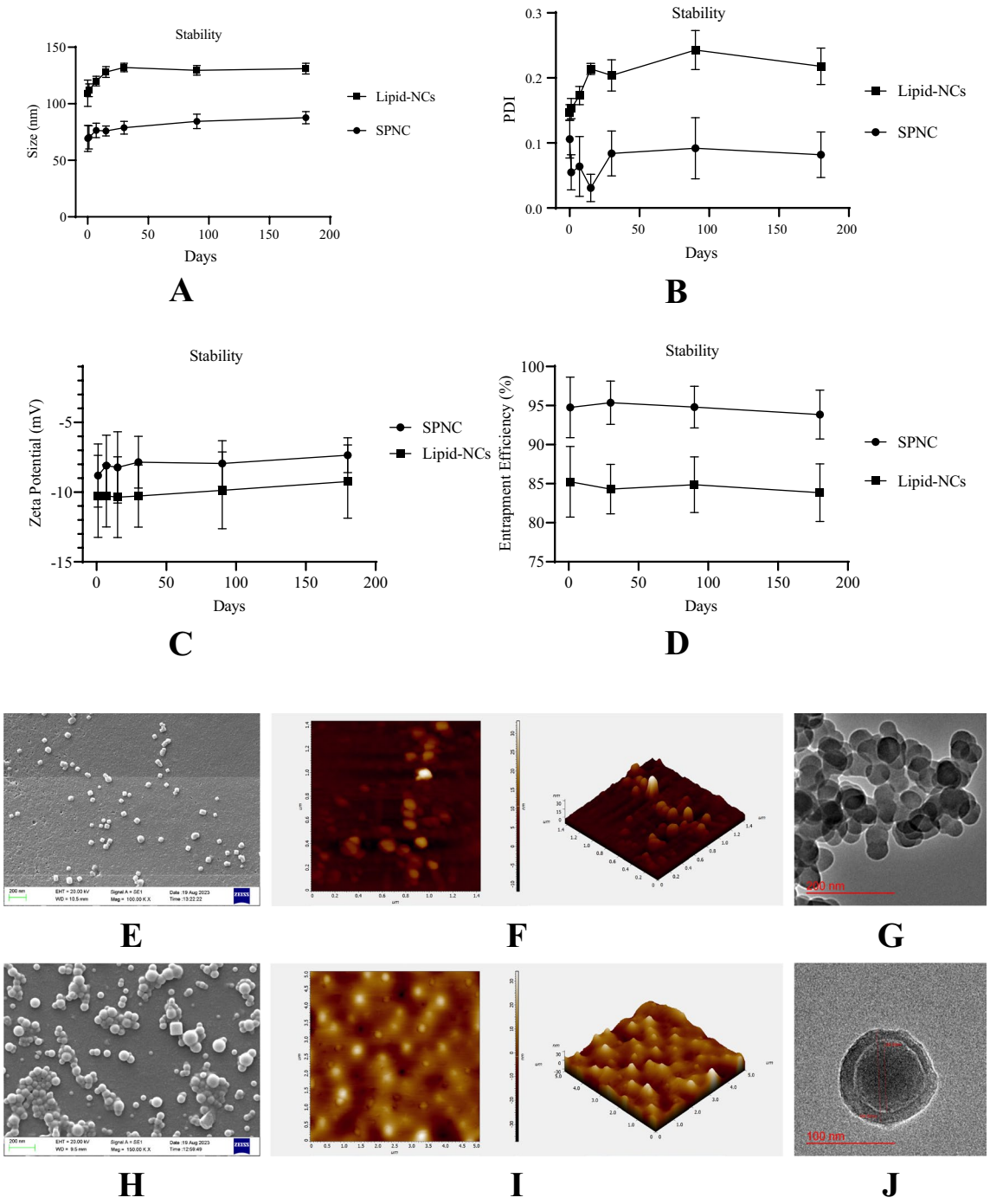

Fig. 2 Stability study graph for particle size (**A**), polydispersity index, PDI (**B**), zeta potential (**C**), and entrapment efficiency (**D**) of SPNC and Lipid-NCs. SEM, AFM and TEM images for SPNC (**E**, **F** & **G**, respectively) and Lipid NCs (**H**, **I** & **J**, respectively)

drug migration from local site to systemic circulation. Therefore, Lipid-NCs were prepared to retard the release providing drug release in controlled manner and at a slower rate than SPNC. The nanocrystals followed logistic (β = 3.48) for SPNC, while both logistic (β = 1.95) and Makoid-Banakar model (n = 0.59 and kMB = 15.5) for Lipid-NCs (Table S1). Similar release kinetic was observed for polymeric nanoparticles [24, 34].

MTT assay was conducted to determine the role of nanocrystals in inducing cell death in MDA-MB 231 cancer cells, as compared to pure PTX (Fig. 5A). Pure PTX and nanocrystals exhibited concentration dependent effect on cell viability. However, the cell cytotoxicity of nanocrystals towards MDA-MB 231 cells was higher. The IC_{50} values observed with pure

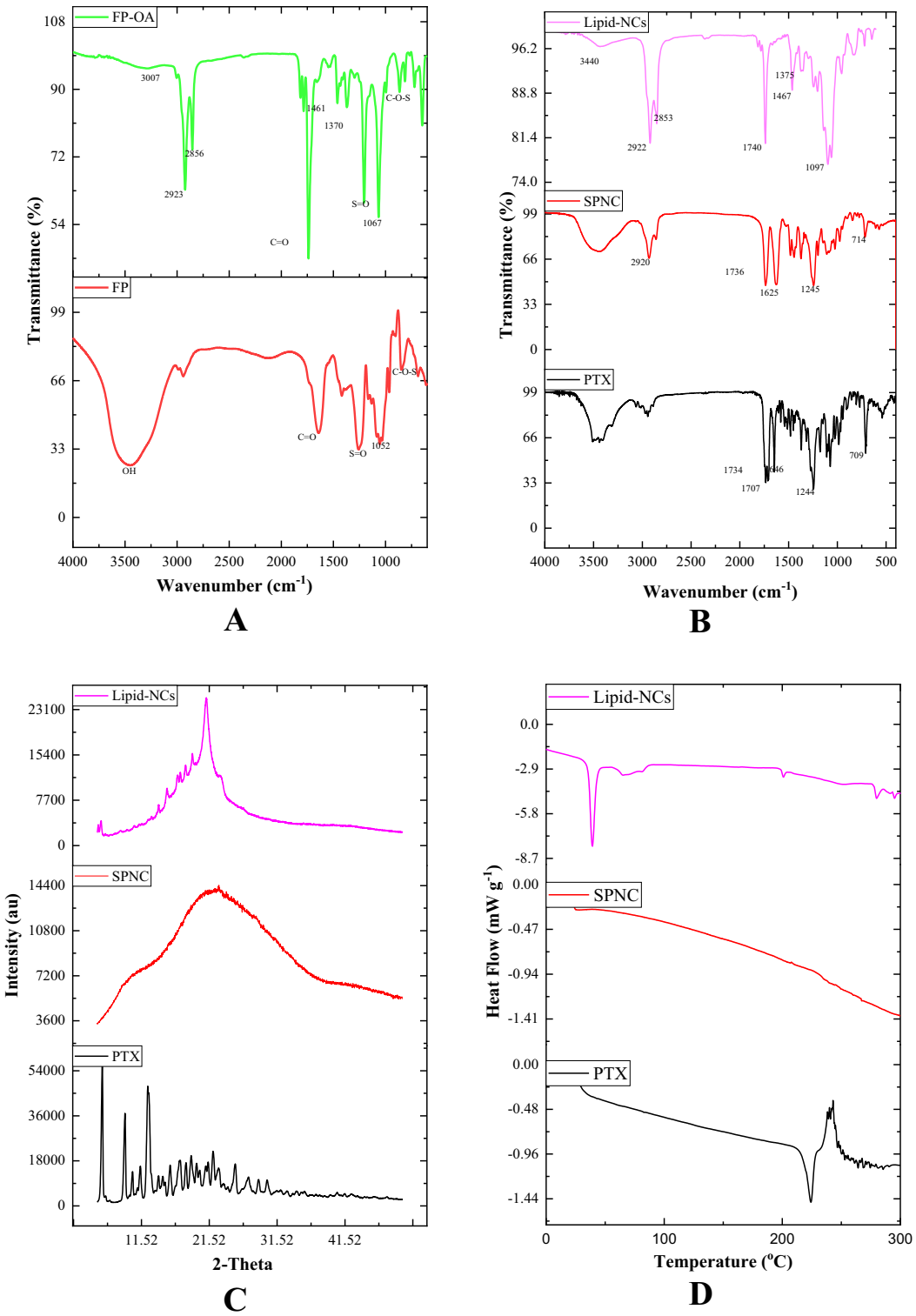

Fig. 3 FTIR spectrum **A** & **B** of fucoidan, fucoidan-oleylamine conjugate, PTX, SPNC, and Lipid-NCs. XRD spectra (**C**), and DSC thermogram **D** of PTX, SPNC and Lipid-NCs

PTX, SPNC, Lipid-NC (without FP-OA) and Lipid-NC (with FP-OA) were 3.89, 2.05, 1.75 and 1.39, respectively. The higher cytotoxicity of nanocrystals could be due to their cellular accumulation potential as compared to pure PTX. However, the cytotoxicity results in MDA-MB 231 cells by SPNC and Lipid-NC (without FP-OA) were close. A slight increase in cell cytotoxicity by Lipid-NC could be due to high membrane interaction of lipid coated nanocrystals. Additionally, the higher

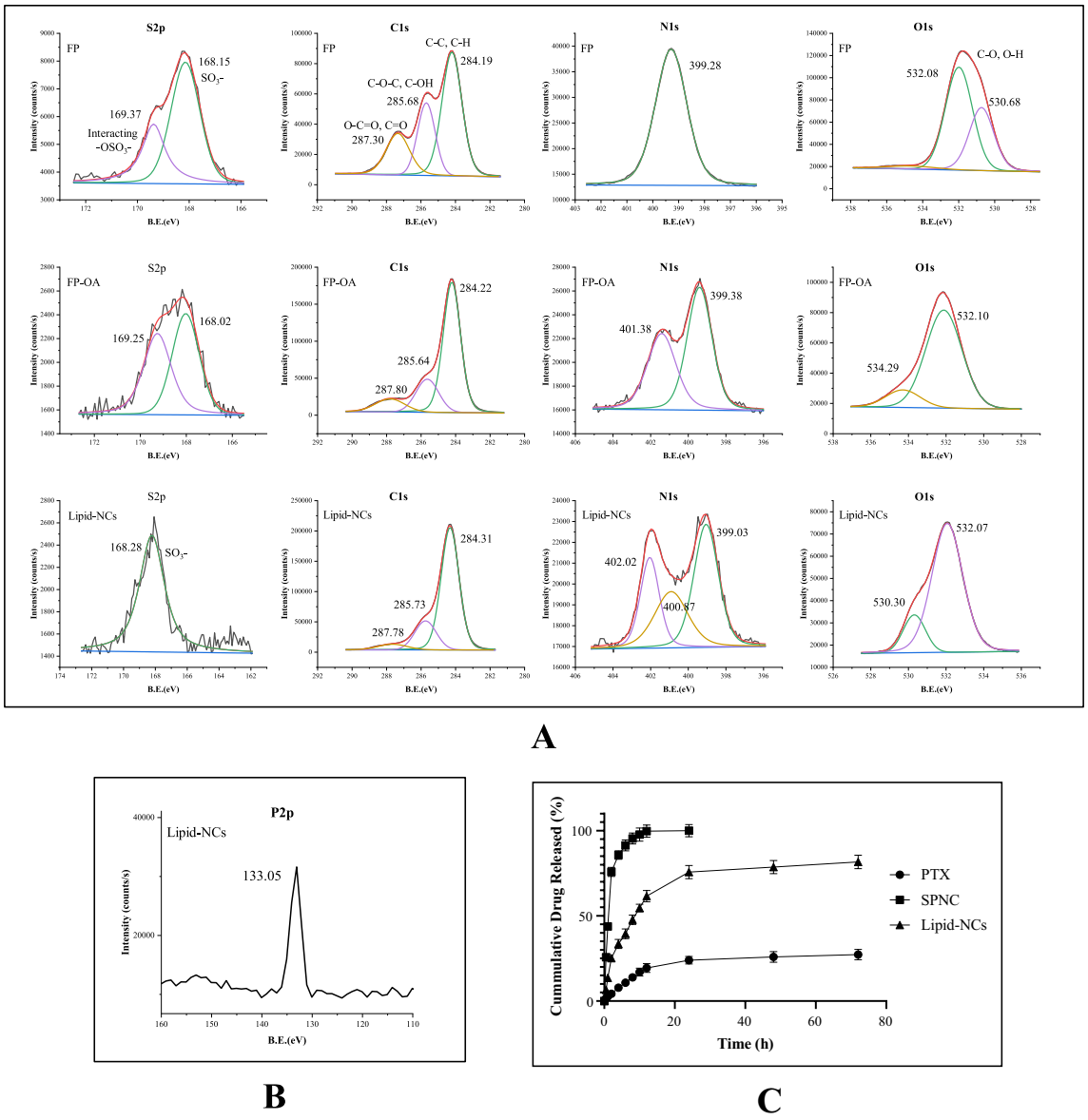

Fig. 4 Deconvulated XPS spectra **A** & **B** of fucoidan (FP), fucoidan-oleylamine conjugate (FP-OA), and Lipid-NCs. In-vitro drug release profile **C** of pure PTX, SPNC and Lipid-NCs

cytotoxicity exhibited by Lipid-NC (with FP-OA) as compared to Lipid-NC (without FP-OA) could be due to fucoidan assisted cellular internalization in cancer cells [35].

The cellular uptake study revealed role of nanocrystals in improving the cellular internalization in MDA-MB-231 cells, as compared to pure drug (Fig. 5B). In free C6-treated groups, a low green fluorescence was observed probably due to internalization-in and efflux-out of free-C6 in MDA-MB-231 cells. As compared to free-C6, a stronger green fluorescence was observed in cells treated nanocrystals attributed to higher cellular internalization potential of nanocrystals. Compared to only-soluplus stabilized nanocrystals (SPNC-C6), Lipid-NCs-C6 (without FP-OA) exhibited a higher green fluorescence attributed to high membrane fluidization potential. Moreover, Lipid-NCs-C6 (with FP-OA) exhibited more stronger green fluorescence than Lipid-NCs-C6 (without FP-OA). This could be due to a higher cellular internalization potential of Lipid-NCs-C6 (with FP-OA) probably due to fucoidan on its surface that facilitated receptor mediated endocytosis of nanocrystals in MDA-MB-231 cells [35].

Apoptosis study through Hoechst 33342/PI dual staining method was conducted for prepared nanocrystals as compared to pure drug (Fig. 6). Control cells exhibited uniform blue fluorescence without any nuclear fragmentation revealing normocellular proliferation of MDA-MB-231 cells. In contrast, pure PTX treated groups signs of nuclear

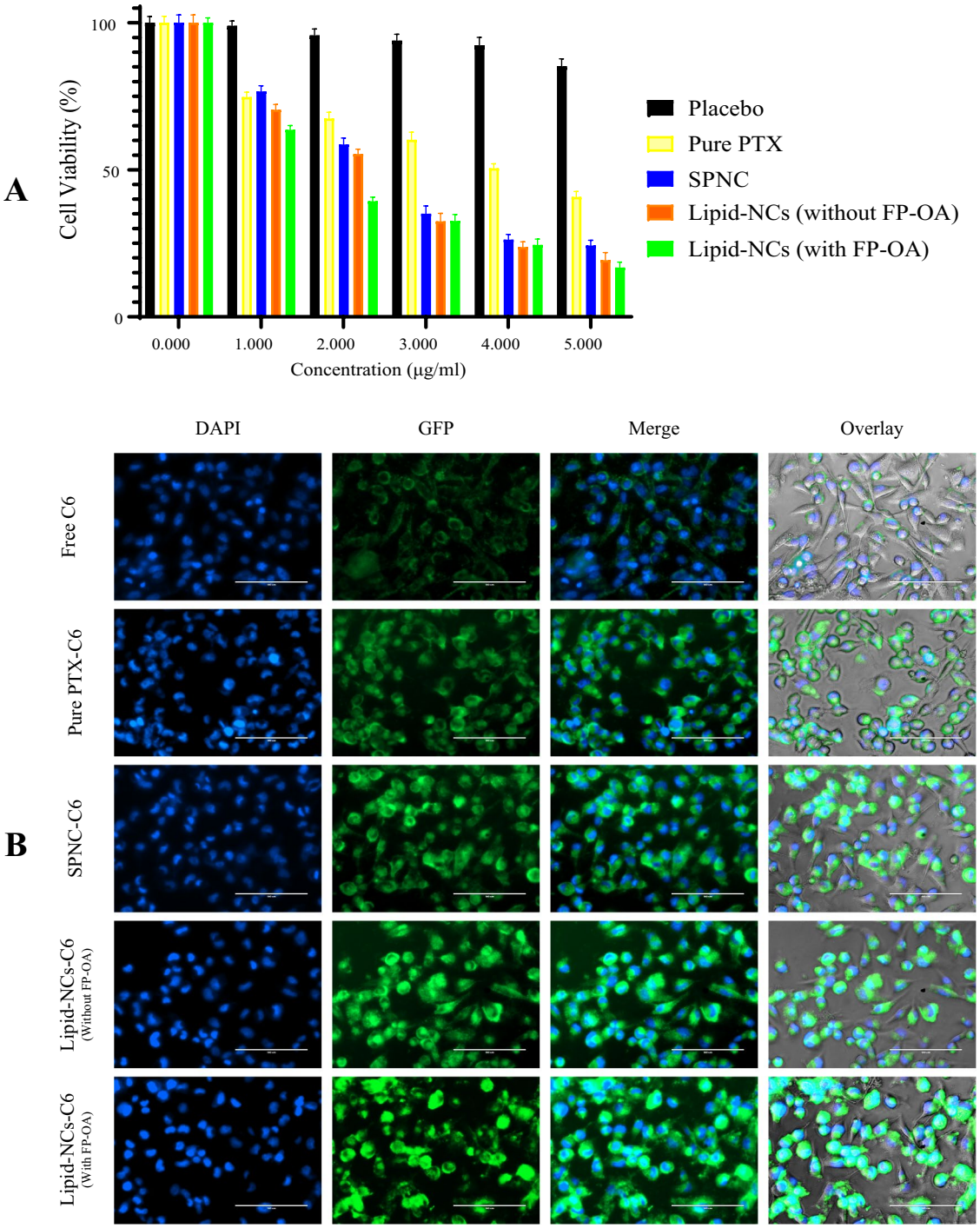

Fig. 5 **A** MTT assay of Placebo, pure PTX, SPNC, Lipid-NCs (without FP-OA) and Lipid-NCs (with FP-OA) in MDA-MB 231 cells. **B** Fluorescence microscopic images for investigating cellular uptake of Free C6, pure PTX-C6, SPNC-C6, Lipid-NCs-C6 (without FP-OA) and Lipid-NCs-C6 (with FP-OA) in MDA-MB 231 cells. Green fluorescence observed due to cytoplasmic uptake while blue fluorescence was for nuclear morphology. Each scale bar represents 100 µm

fragmentation attributed to apoptosis induction potential of PTX. Compared to this, nanocrystals treated groups showed more apoptotic cells due to their higher internalization responsible for more nuclear fragmentation and chromatin condensation. Additionally, the number of late apoptotic cells were higher in Lipid-NCs attributed to fucoidan driven receptor mediated endocytosis in MDA-MB-231 cells. The results suggested the higher potency of prepared nanocrystals in inducing apoptosis and thus cancer cell death, as compared to pure PTX.

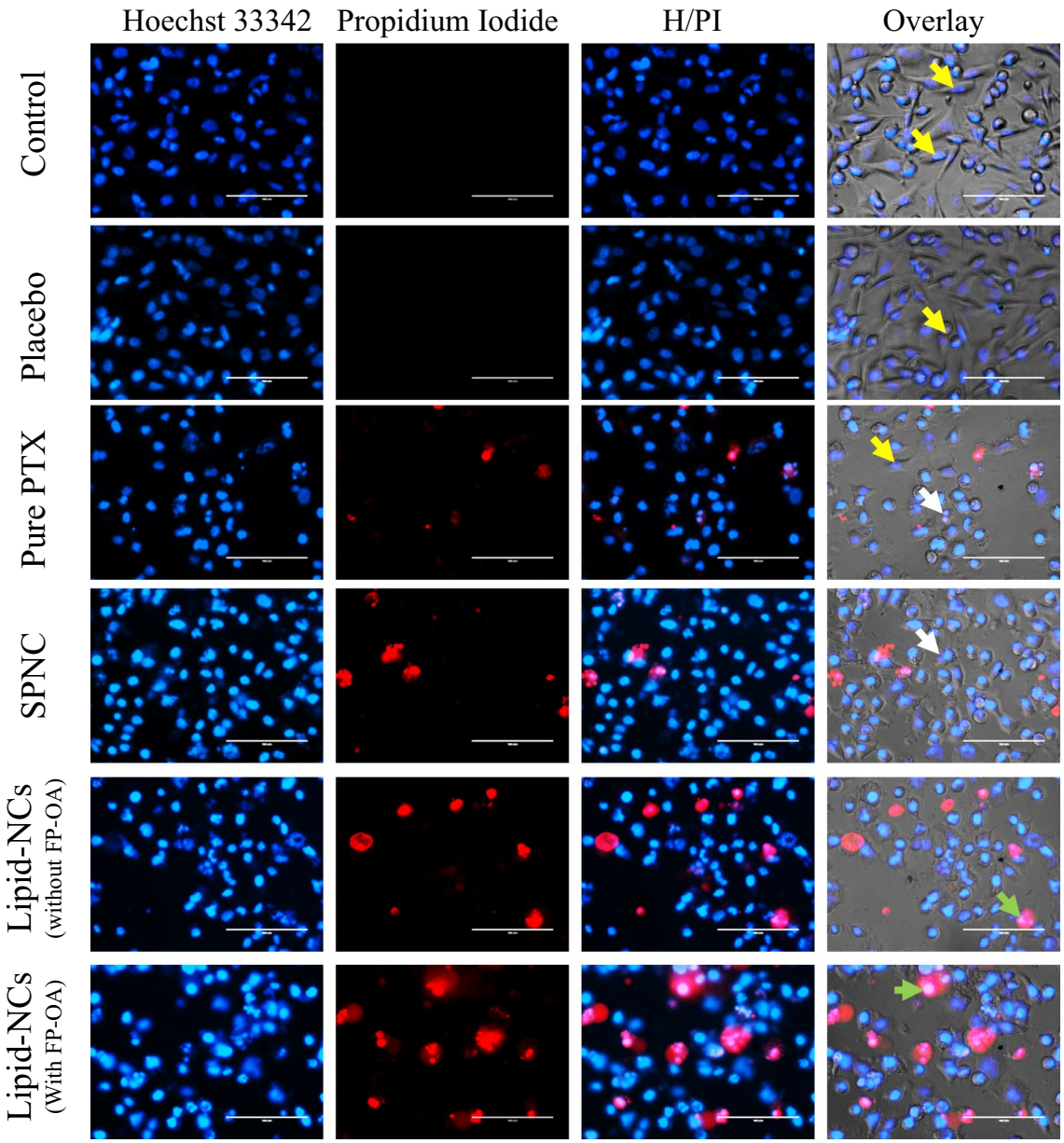

Fig. 6 Assessment of apoptotic nuclear morphological changes post-treatment to Placebo, pure PTX, SPNC, Lipid-NCs (without FP-OA), and Lipid-NCs (with FP-OA) through Hoechst 33342/PI dual staining method, compared to Control. Yellow, white, and green arrows indicated live, early apoptotic, and late apoptotic cells, respectively

3.3 Evaluation of injectable hydrogels

The injectable hydrogel was successfully prepared by cold method. The microscopic analysis revealed large porous hydrogel (Fig. 7A and B) that upon addition of nanocrystals dispersion get filled. The nanocrystals were observed entrapped and embedded in hydrogel with few on surface of hydrogel, as confirmed by SEM (Fig. 7C and E). The nanocrystals were observed to get homogeneously dispersed throughout the hydrogel as observed in AFM (Fig. 7D and F). Prepared injectable hydrogel was evaluated for sol–gel transition, syringe ability and rheology. Prepared hydrogel retained its sol form at lower temperature (2–8 ℃) and attained gel-form at a higher temperature (about 29–37 °C). Drug-free hydrogel exhibited sol–gel transition at 35.4 ℃ while PTX Gel showed transition at 29.8 ℃. SPNC Gel and Lipo-NCs Gel exhibited sol–gel transition at 31.8 ℃ and 33.2 ℃, respectively. The viscosity of hydrogel was determined in sol- and gel-form. The viscosity of sol-form was 0.055 ± 0.56, 0.076 ± 0.85 and 0.073 ± 0.94 Pa/s

for drug-free, drug loaded and NCs-loaded hydrogel, respectively. In case of gel form, the transition in viscosity to 5.50 ± 0.24, 7.95 ± 0.61 Pa/s and 7.26 ± 0.37 Pa/s for drug free, drug-loaded and NCs loaded hydrogel, respectively (Fig. S3). The lower viscosity values of sol-phase showed suitability of prepared hydrogel for injection through needle. While higher viscosity of gel form was due to sol–gel transition at temperature of body tissues (25–37 °C) upon injection of hydrogel sol to consequently form the 3D networks gel. The vial tilting method showed gelation of sol to gel within 5 min at room temperature (25 ℃) (Fig. 7G). However, the gelation occurred in less than 2 min at 37 ℃. Therefore, prepared hydrogel had a adequate sol–gel transition time span to facilitate the smooth transfer of gel from vial to intratumoral injection site. The prepared hydrogel (sol-form) easily injected out of the syringe, thereby exhibiting high syringeability (Fig. 7H). The in-situ hydrogel was also evaluated visually before and after gelation, revealing smooth and uniform gel formation without the sign of any phase separation in both sol and gel forms. The color of in-situ gel was clear and colorless for drug and nanocrystals-free hydrogel while exhibited turbid white in case of drug and nanocrystals loaded hydrogel (Fig. 7G). The pH of hydrogel was around 6.70 ± 0.21 and was within the range (pH 6.5–7.4 for injectable hydrogels) suitable for subcutaneous injection to avoid tissue irritation. The drug content of the prepared hydrogel was 95.20 ± 2.91% and 89.58 ± 2.76% for SPNC Gel and Lipid-NCs Gel, respectively. The nanocrystals were observed to uniformly dispersed in the hydrogel base.

Drug release study was further conducted to determine the release of drug from hydrogel at pH 6.8 (Fig. 7I and Table S1). PTX-Gel showed drug release of only 18.90 ± 2.12 in 24 h and 27.48 ± 2.87% in 72 h. The slow drug release could be due to poor solubility of drug. Pure PTX-Gel followed Gompertz model (β = 0.56) suggesting slow drug release via diffusion mechanism from hydrogels [36, 37]. SPNC-Gel showed drug release at a higher rate showing 83.04 ± 3.84% PTX release in 24 h, followed by 99.64 ± 3.87% in 72 h. The higher drug release was attributed to high solubility and permeability potential of nanocrystals. In contrast, Lipid-NCs Gel exhibited controlled drug release showing 69.20 ± 2.84% in 24 h and 82.94 ± 3.29% in 72 h. SPNC-Gel and Lipid-NCs Gel followed Weibull Model (β = 3.94 for SPNC and 4.14 for Lipid-NCs) suggesting controlled drug release via diffusion mechanism [38]. The Weibull function may result from the formation of a concentration gradient near the releasing borders of hydrogel matrix [39].

3.4 In vivo *studies*

In vivo studies for determining the efficacy of PTX Gel and Lipid-NCs Gel as compared to PTX (i.v.) were conducted. The change in tumor volume was determined showing significantly ($p < 0.0001$) higher tumor volume inhibition by Lipid-NCs Gel compared to PTX Gel and PTX (i.v.) (Fig. 8A). This could be due to higher penetration potential of nanoparticles and availability of major drug fraction near the tumor area. The tumor volume reduction compared to untreated group was 52%, 65% and 93% by PTX (i.v.), PTX Gel and Lipid-NCs Gel, respectively at day 14. The tumor volume treated with Lipid-NCs Gel observed to decrease with time during the course of treatment. This could be attributed to higher release and tumor penetration of Lipid-NCs from hydrogel. Lipid-NCs released from hydrogel can easily internalize the cancer cells via endocytosis to exert the anti-tumor effect. In contrast, the tumor volume increased for groups treated with PTX (i.v.) and PTX Gel. Lower control on tumor growth was attributed to low regioselective delivery of drug from PTX (i.v.) owing to off target distribution, while due to slow release of free drug from PTX Gel. However, compared to untreated group, PTX (i.v.) and PTX Gel had significant control over tumor growth. Additionally, PTX Gel had a higher tumor inhibition than PTX (i.v.) that could be due to localized drug delivery from hydrogel. However, as observed in Fig. 8B, PTX (i.v.) and PTX Gel still showed the mass formation (yellow arrow), cell proliferation (red arrow) and mucin production (green arrow) as signs of cancer. These signs were absent in Lipid-NCs Gel treated groups revealing its higher efficacy in treatment of tumor.

The body weight was also measured for groups treated with PTX (i.v.), PTX Gel and Lipid-NCs Gel and compared with Normal SD rats and untreated tumor bearing SD rats (Fig. 8C). The positive change in body weight was observed in tumor bearing SD rats as compared to healthy Normal SD rats that may be attributed to the rapidly increasing tumor volume. In contrast, Negative change in body weight was observed for PTX (i.v.) treated groups that could be due to drug related toxicity. Whereas, no change in body weight for Lipid-NCs Gel treated groups was observed and the trend followed Normal SD rats, suggesting the role of lipid nanocrystals in tumor inhibition. PTX Gel also found to initially control the tumor growth, however an increase in body weight was observed later.

The survival rate of all groups including PTX (i.v.), PTX Gel, Lipid-NCs Gel, Normal SD rats and untreated tumor bearing SD rats was also determined (Fig. 8D). The survival rate of Lipid-NCs Gel was higher compared to untreated tumor bearing rats, PTX (i.v.) and PTX Gel treated groups. The median survival period was 41, 54, 112, and > 120 days for untreated tumor bearing rats, PTX (i.v.), PTX Gel, and Lipid-NCs Gel. The improved survival rate of PTX Gel and Lipid-NCs treated groups

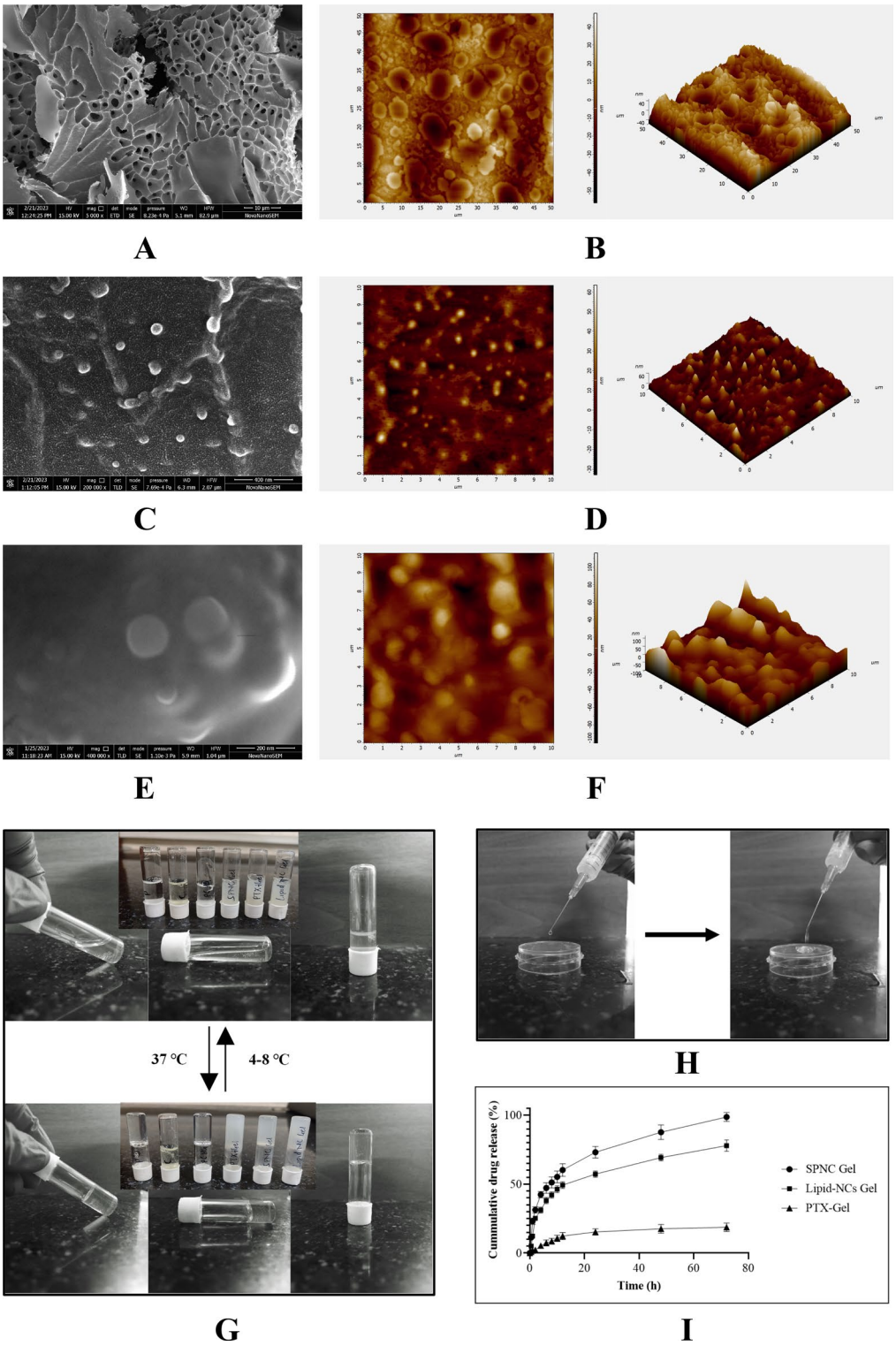

Fig. 7 SEM and AFM micrographs of drug free hydrogel (**A** & **B**), SPNC gel (**C** & **D**), and Lipid-NCs gel (**E** & **F**). Sol-Gell transition assessment via vial tilt method (**G**). Syringeability analysis of gel (**H**), and in vitro drug release profile (**I**) of pure PTX gel, SPNC gel, and Lipid-NCs gel

was attributed to lower toxicity and higher efficacy of nanoparticles loaded hydrogel. Overall, the improved antitumor efficacy of drug by lipid-nanocrystals was responsible for tumor inhibition and prolonged survival period probably due to maximum drug accumulation at target site, higher drug penetration potential in complex tumor tissues attributed to their size and cellular internalization exploiting fucoidan guided integrin-receptor mediated endocytosis.

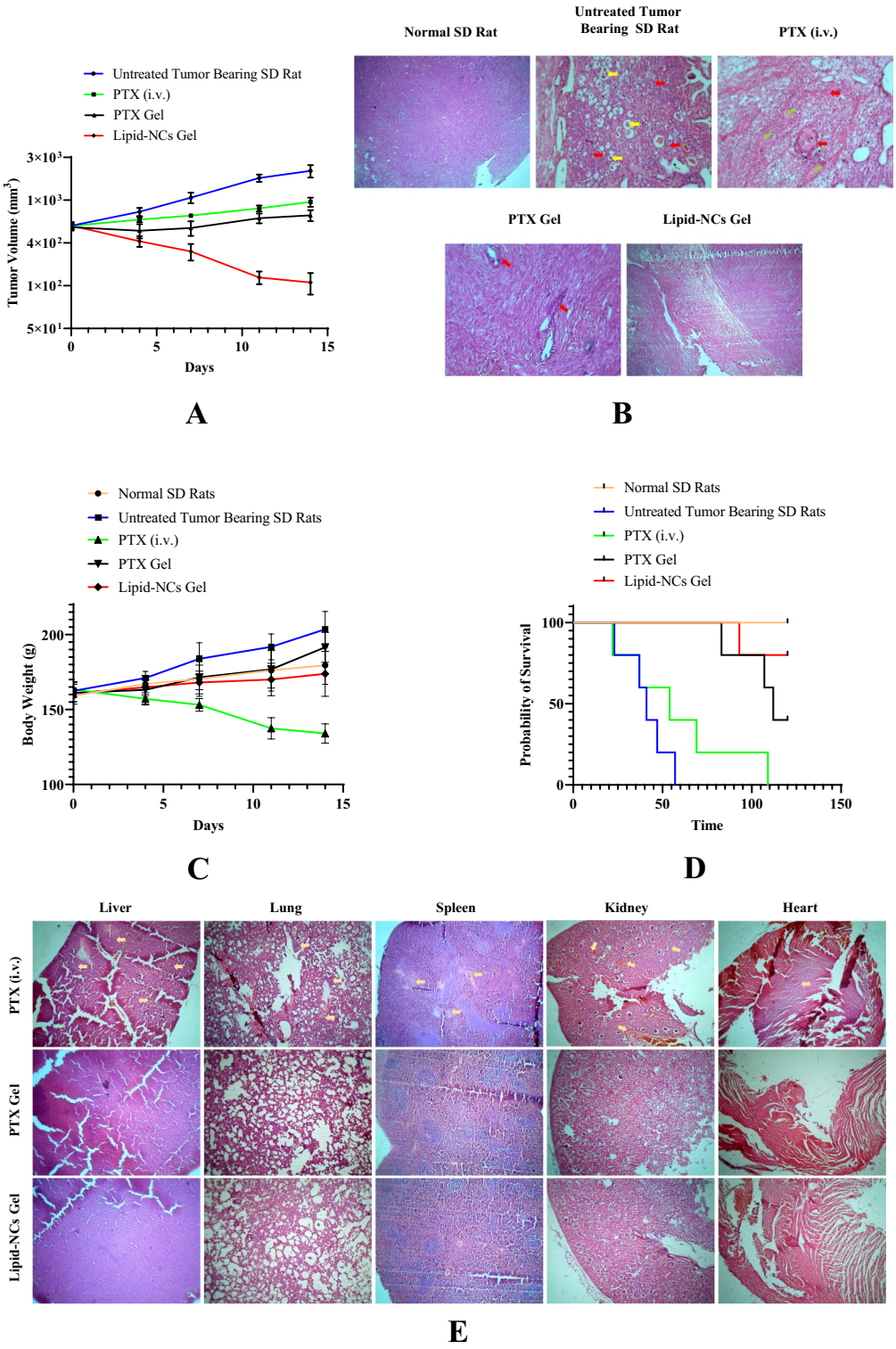

Fig. 8 In vivo studies of prepared injectable hydrogel. **A** tumor regression analysis of DMBE induced tumor bearing rats, tumor volume of PTX (i.v.), PTX gel, and Lipid-NCs gel treated rats compared to untreated tumor bearing rats. **B** Histological images of H&E stained healthy/tumor tissues collected at day 14. **C** Body weight of PTX (i.v.), PTX gel, and Lipid-NCs gel treated rats compared to untreated tumor bearing rats and normal SD rats. **D** Kaplan–Meier survival probability plot of normal SD rats, untreated tumor bearing rats, PTX (i.v.), PTX gel, and Lipid-NCs gel treated rats. **E** H&E-stained histological images of all major organs (including liver, lung, spleen, kidney and heart) of rats treated with PTX (i.v.), PTX gel, and Lipid-NCs (Magnification = 4X)

Histological analysis of all major organs showed no signs of systemic toxicity when treated with Lipid-NCs Gel. The localized delivery of PTX from injectable hydrogel probably restricted the drug distribution to major organs, thereby minimizing the systemic toxicity. In contrary to this, intravenous administered PTX showed signs of organ toxicity (Fig. 8E, yellow arrow) due to drug distribution to all major organs. Therefore, prepared nanocrystals loaded hydrogel emerged as a promising carrier for safe and effective delivering of PTX to treat breast cancer.

4 Conclusion

Localized drug delivery using thermosensitive hydrogels have become a promising strategy in cancer therapy, avoiding systemic side effects and improving drug efficacy. Exploiting this approach, a thermosensitive hydrogel consisting of chitosan and pluronic F127 was prepared for anticancer drug delivery near tumoral site in sol-form that converts to gel-form at microenvironment temperature. To improve the release of hydrophobic PTX from hydrogel and maintain local drug concentration, PTX was formulated as nanocrystals. Additionally, nanocrystals were lipid coated to provide controlled drug release, retain drug at target site and improve cellular internalization for better anti-tumor effect. Prepared nanocrystals were then loaded in hydrogel (Lipid-NCs-Gel) and evaluated for in vitro and in vivo examinations. The results showed that prepared nanocrystal loaded hydrogel had a clear, regular network structure with high thermosensitivity, good syringeability, suitable rheology and acceptable pH. The hydrogel exhibited promising sol–gel transition behavior at body temperature within two minutes. In vivo studies revealed the role of nanocrystals assembled hydrogel in tumor inhibition and thus prolonging survival period. Prepared hydrogel thus can be employed as a powerful auxiliary medication in localized drug delivery for tumour inhibition and breast cancer management.

Development of BCS Class IV anticancer drug nanocrystals loaded hydrogel system, with its innovative design and function, might offer significant potential for clinical translation, especially in the context of breast cancer therapy. It permits localized intratumoral drug delivery that minimizes systemic toxicity, thus improving the therapeutic index of paclitaxel (PTX) and overcoming the major drawback of traditional chemotherapy. The thermosensitive sol–gel transition at physiological temperatures can enable easy administration, with stable retention at the target site. The profile of drug release from the hydrogel ensures continued availability of drugs at the site of the tumor for better therapeutic action. Despite its promise, taking this technology from bench to bedside faces several scalability challenges. The process of fabricating lipid nanocrystals to produce homogeneously stable nanocrystals at the industrial scale is quite challenging and very stringently controlled in the processing. Batch-to-batch variation may pose consistent sol–gel transition properties for large-scale manufacture. The multi-component nature of the system (lipid coating, conjugate modifications, and hydrogel matrix) makes it challenging to get regulatory approval because each component must be carefully assessed for safety and efficacy. The integration of advanced nanotechnology with specialized biomaterials may make the product more expensive, thereby limiting access. The stability of the hydrogel and nanocrystals on thermosensitive changes at different storage conditions must be investigated. Future studies may focus on pharmacokinetics and biodistribution in understanding drug release profiles, systemic absorption, and long-term safety in cancer models. Co-loading ability of hydrogel with multiple therapeutic agents like immunotherapies or synergistic drugs can be investigated. In vivo performance of the system in heterogeneous tumor environments or under conditions that mimic patient variability could be studied. In conclusion, although lipid nanocrystal-loaded hydrogel represents a cutting-edge platform for localized cancer therapy, addressing scalability and regulatory issues, as well as conducting additional research, can considerably increase its clinical application.

Acknowledgements Authors are thankful to Central Instrumentation Facility (CIF) IIT(BHU), Varanasi for providing the instruments and facilities for nano-formulations characterization.

Author contributions MK and BM conceptualize the manuscript and methodology. MK and AJ did the investigation, data curation, validation, formal analysis, writing the original draft, and revisions. PG did in vitro cell line studies, data curation, and manuscript writing. RS, MM, and KB contributed to data curation, software analysis, and visualization of data. BK provided resources for in vitro cell line experiments, software, and did manuscript editing. BM supervised the experiments, provided resources and software, and did review & editing of the manuscript.

Data availability Data is provided within the manuscript or supplementary information files (Figs. S1, S2, S3 and S4 and Tables S1 and S2).

Declarations

Competing interests The authors declare no competing interests.

References

1. Xu Y, Gong M, Wang Y, Yang Y, Liu S, Zeng Q. Global trends and forecasts of breast cancer incidence and deaths. Sci Data. 2023;10:334. https://doi.org/10.1038/s41597-023-02253-5.
2. Kwak S-B, Kim SJ, Kim J, Kang Y-L, Ko CW, Kim I, Park J-W. Tumor regionalization after surgery: roles of the tumor microenvironment and neutrophil extracellular traps. Exp Mol Med. 2022;54:720–9. https://doi.org/10.1038/s12276-022-00784-2.
3. Chen Z, Zhang P, Xu Y, Yan J, Liu Z, Lau WB, Lau B, Li Y, Zhao X, Wei Y, Zhou S. Surgical stress and cancer progression: the twisted tango. Mol Cancer. 2019;18:132. https://doi.org/10.1186/s12943-019-1058-3.
4. Alieva M, van Rheenen J, Broekman MLD. Potential impact of invasive surgical procedures on primary tumor growth and metastasis. Clin Exp Metastasis. 2018;35:319–31. https://doi.org/10.1007/s10585-018-9896-8.
5. Vasan N, Baselga J, Hyman DM. A view on drug resistance in cancer. Nature. 2019;575:299–309. https://doi.org/10.1038/s41586-019-1730-1.
6. Basak D, Arrighi S, Darwiche Y, Deb S. Comparison of anticancer drug toxicities: paradigm shift in adverse effect profile. Life. 2021;12:48. https://doi.org/10.3390/life12010048.
7. Minchinton AI, Tannock IF. Drug penetration in solid tumours. Nat Rev Cancer. 2006;6:583–92. https://doi.org/10.1038/nrc1893.
8. Fan R, Cheng Y, Wang R, Zhang T, Zhang H, Li J, Song S, Zheng A. Thermosensitive hydrogels and advances in their application in disease therapy. Polymers. 2022;14:2379. https://doi.org/10.3390/polym14122379.
9. Liu J, Zhang L, Yang Z, Zhao X. Controlled release of paclitaxel from a self-assembling peptide hydrogel formed in situ and antitumor study in vitro. Int J Nanomed. 2011;6:2143–53. https://doi.org/10.2147/IJN.S24038.
10. Mikhail AS, Morhard R, Mauda-Havakuk M, Kassin M, Arrichiello A, Wood BJ. Hydrogel drug delivery systems for minimally invasive local immunotherapy of cancer. Adv Drug Deliv Rev. 2023;202: 115083. https://doi.org/10.1016/j.addr.2023.115083.
11. Xin H, Naficy S. Drug delivery based on stimuli-responsive injectable hydrogels for breast cancer therapy: a review. Gels. 2022;8:45. https://doi.org/10.3390/gels8010045.
12. Ma Q, Li Q, Cai X, Zhou P, Wu Z, Wang B, Ma W, Fu S. Injectable hydrogels as drug delivery platform for in-situ treatment of malignant tumor. J Drug Deliv Sci Technol. 2022;76: 103817. https://doi.org/10.1016/j.jddst.2022.103817.
13. Ohya Y. Temperature-responsive biodegradable injectable polymer systems with conveniently controllable properties. Polym J. 2019;51:997–1005. https://doi.org/10.1038/s41428-019-0217-0.
14. Zhang B, Xue A, Zhang C, Yu J, Chen W, Sun D. Bile salt liposomes for enhanced lymphatic transport and oral bioavailability of paclitaxel. Pharm. 2016;71:320–6.
15. Dyett BP, Yu H, Strachan J, Drummond CJ, Conn CE. Fusion dynamics of cubosome nanocarriers with model cell membranes. Nat Commun. 2019;10:4492. https://doi.org/10.1038/s41467-019-12508-8.
16. Alwarsamy M, Gooneratne R, Ravichandran R. Effect of fucoidan from Turbinaria conoides on human lung adenocarcinoma epithelial (A549) cells. Carbohydr Polym. 2016;152:207–13. https://doi.org/10.1016/j.carbpol.2016.06.112.
17. Kumar M, Shanthi N, Mahato AK, Soni S, Rajnikanth PS. Preparation of luliconazole nanocrystals loaded hydrogel for improvement of dissolution and antifungal activity. Heliyon. 2019;5: e01688. https://doi.org/10.1016/j.heliyon.2019.e01688.
18. Kumar M, Jha A, Bharti K, Manjit M, Kumbhar P, Dhapte-Pawar V, Mishra B. Lipid-coated nanocrystals of paclitaxel as dry powder for inhalation: characterization, in-vitro performance, and pharmacokinetic assessment. Colloids Surf B Biointerfaces. 2024;237: 113865. https://doi.org/10.1016/j.colsurfb.2024.113865.
19. Ruttala HB, Ko YT. Liposome encapsulated albumin-paclitaxel nanoparticle for enhanced antitumor efficacy. Pharm Res. 2015;32:1002–16. https://doi.org/10.1007/s11095-014-1512-2.
20. García-Couce J, Tomás M, Fuentes G, Que I, Almirall A, Cruz LJ. Chitosan/Pluronic F127 thermosensitive hydrogel as an injectable dexamethasone delivery carrier. Gels. 2022;8:44. https://doi.org/10.3390/gels8010044.
21. Wang M, Chen J, Li W, Zang F, Liu X, Qin S. Paclitaxel-nanoparticles-loaded double network hydrogel for local treatment of breast cancer after surgical resection. Mater Sci Eng C. 2020;114: 111046. https://doi.org/10.1016/j.msec.2020.111046.
22. Abdellatif AAH, Mohammed AM, Saleem I, Alsharidah M, Al Rugaie O, Ahmed F, Osman SK. smart injectable chitosan hydrogels loaded with 5-fluorouracil for the treatment of breast cancer. Pharmaceutics. 2022;14(3):661. https://doi.org/10.3390/pharmaceutics14030661.
23. Bharadwaj R, Das PJ, Pal P, Mazumder B. Topical delivery of paclitaxel for treatment of skin cancer. Drug Dev Ind Pharm. 2016;42:1482–94. https://doi.org/10.3109/03639045.2016.1151028.
24. Jha A, Kumar M, Goswami P, Manjit M, Bharti K, Koch B, Mishra B. Hyaluronic acid-oleylamine and chitosan-oleic acid conjugate-based hybrid nanoparticle delivery via. Dissolving microneedles for enhanced treatment efficacy in localized breast cancer. Biomater Adv. 2024;160:213865. https://doi.org/10.1016/j.bioadv.2024.213865.
25. Kołodziejczak-Radzimska A, Bielejewski M, Biadasz A, Jesionowski T. Evaluation of MxOy/fucoidan hybrid system and their application in lipase immobilization process. Sci Rep. 2022;12:7218. https://doi.org/10.1038/s41598-022-11319-0.
26. Reys LL, Silva SS, Soares da Costa D, Rodrigues LC, Reis RL, Silva TH. Building fucoidan/agarose-based hydrogels as a platform for the development of therapeutic approaches against diabetes. Molecules. 2023;28:4523. https://doi.org/10.3390/molecules28114523.

27. Zayed A, El-Aasr M, Ibrahim A-RS, Ulber R. Fucoidan characterization: determination of purity and physicochemical and chemical properties. Mar Drugs. 2020;18:571. https://doi.org/10.3390/md18110571.
28. Lai Y-H, Chiang C-S, Hsu C-H, Cheng H-W, Chen S-Y. Development and characterization of a fucoidan-based drug delivery system by using hydrophilic anticancer polysaccharides to simultaneously deliver hydrophobic anticancer drugs. Biomolecules. 2020;10:970. https://doi.org/10.3390/biom10070970.
29. Li C, Zhang G, Xun L, Liu D, Wang M. Depressant behavior of crude fucoidan in the separation of talc and molybdenite. Colloids Surf Physicochem Eng Asp. 2022;651: 129645. https://doi.org/10.1016/j.colsurfa.2022.129645.
30. de Sousa Marcial SP, Carneiro G, Leite EA. Lipid-based nanoparticles as drug delivery system for paclitaxel in breast cancer treatment. J Nanoparticle Res. 2017;19:340. https://doi.org/10.1007/s11051-017-4042-0.
31. Amin MdL, Mawad D, Dokos S, Koshy P, Martens PJ, Sorrell CC. Fucoidan- and carrageenan-based biosynthetic poly(vinyl alcohol) hydrogels for controlled permeation. Mater Sci Eng C. 2021;121: 111821. https://doi.org/10.1016/j.msec.2020.111821.
32. Li Z, Qiao W, Wang C, Wang H, Ma M, Han X, Tang J. DPPC-coated lipid nanoparticles as an inhalable carrier for accumulation of resveratrol in the pulmonary vasculature, a new strategy for pulmonary arterial hypertension treatment. Drug Deliv. 2020;27:736–44. https://doi.org/10.1080/10717544.2020.1760962.
33. Kumar M, Goswami P, Jha A, Manjit M, Satpute AP, Koch B, Mishra B. Formulation and evaluation of cetuximab functionalized phospholipid modified nanocrystals of paclitaxel for non-small cell lung cancer therapy. Sci Rep. 2024;14:29114. https://doi.org/10.1038/s41598-024-80283-8.
34. Jha A, Goswami P, Kumar M, Bharti K, Manjit M, Satpute AP, Gupta A, Moorkoth S, Koch B, Mishra B. Cetuximab functionalized chitosan/hyaluronic acid-based nanoparticles loaded with cabazitaxel enhances anti-tumor efficacy in DMBA-induced breast cancer model in rats through spatial targeting, Chem. Phys. Impact (2024) 100750. https://www.sciencedirect.com/science/article/pii/S2667022424002949 (accessed November 5, 2024).
35. Jafari M, Sriram V, Xu Z, Harris GM, Lee J-Y. Fucoidan-doxorubicin nanoparticles targeting p-selectin for effective breast cancer therapy. Carbohydr Polym. 2020;249: 116837. https://doi.org/10.1016/j.carbpol.2020.116837.
36. Craciun A-M, Barhalescu ML, Agop M, Ochiuz L. Theoretical modeling of long-time drug release from nitrosalicyl-imine-chitosan hydrogels through multifractal logistic type laws. Comput Math Methods Med. 2019;2019:4091464. https://doi.org/10.1155/2019/4091464.
37. Zhang S, Fan X, Zhang G, Wang W, Yan L. Preparation, characterization, and in vitro release kinetics of doxorubicin-loaded magnetosomes. J Biomater Appl. 2022;36:1469–83. https://doi.org/10.1177/08853282211060544.
38. Özdal ZD, Gültekin Y, Vural İ, Takka S. Development and characterization of polymeric nanoparticles containing ondansetron hydrochloride as a hydrophilic drug. J Drug Deliv Sci Technol. 2022;74: 103599. https://doi.org/10.1016/j.jddst.2022.103599.
39. Papadopoulou V, Kosmidis K, Vlachou M, Macheras P. On the use of the Weibull function for the discernment of drug release mechanisms. Int J Pharm. 2006;309:44–50. https://doi.org/10.1016/j.ijpharm.2005.10.044.